Nano-Micro Lett. (2018) 10:30
https://doi.org/10.1007/s40820-017-0183-z

ARTICLE

Reduced Graphene Oxide-Wrapped FeS_2 Composite as Anode for High-Performance Sodium-Ion Batteries

Qinghong Wang[1] · Can Guo[1] · Yuxuan Zhu[1] · Jiapeng He[1] · Hongqiang Wang[2]

Received: 15 October 2017 / Accepted: 28 November 2017 / Published online: 27 December 2017

Highlights

- Reduced graphene oxide-wrapped FeS_2 (FeS_2/rGO) composite was synthesized by a facile two-step method.
- The integral reduced graphene oxide networks not only connect the FeS_2 nanoparticles but also prevent them from aggregating.
- As anodes for sodium-ion batteries, the FeS_2/rGO composite delivers high specific capacity and good cycling stability.

Abstract Iron disulfide is considered to be a potential anode material for sodium-ion batteries due to its high theoretical capacity. However, its applications are seriously limited by the weak conductivity and large volume change, which results in low reversible capacity and poor cycling stability. Herein, reduced graphene oxide-wrapped FeS_2 (FeS_2/rGO) composite was fabricated to achieve excellent electrochemical performance via a facile two-step method. The introduction of rGO effectively improved the conductivity, BET surface area, and structural stability of the FeS_2 active material, thus endowing it with high specific capacity, good rate capability, as well as excellent cycling stability. Electrochemical measurements show that the FeS_2/rGO composite had a high initial discharge capacity of 1263.2 mAh g^{-1} at 100 mA g^{-1} and a high discharge capacity of 344 mAh g^{-1} at 10 A g^{-1}, demonstrating superior rate performance. After 100 cycles at 100 mA g^{-1}, the discharge capacity remained at 609.5 mAh g^{-1}, indicating the excellent cycling stability of the FeS_2/rGO electrode.

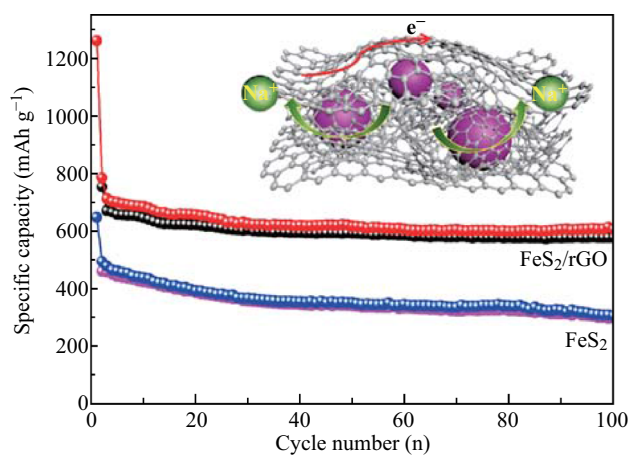

Keywords FeS_2 · Reduced graphene oxide (rGO) · Enwrapping structure · Anode material · Sodium-ion battery

✉ Qinghong Wang
wangqh@jsnu.edu.cn

Hongqiang Wang
hqwanghbu@163.com

[1] School of Chemistry and Chemical Engineering, Jiangsu Key Laboratory of Green Synthetic Chemistry for Functional Materials, Jiangsu Normal University, Xuzhou, Jiangsu 221116, People's Republic of China

[2] College of Chemistry and Environmental Science, Hebei University, Baoding, Hebei 071002, People's Republic of China

1 Introduction

Sodium-ion batteries (SIBs) have been considered to be promising candidates for large-scale energy storage systems, electric vehicles, and other portable devices because of their outstanding electrochemical performance and inexpensive characterization. As the most important parts of SIBs, electrolytes and electrodes have been extensively investigated. It has been demonstrated that polymer electrolytes (such as gel polymer electrolytes and ceramic electrolytes) may be desirable alternatives for liquid electrolytes because of their modularity and reliability in electrochemical devices [1, 2]. Various cathodes, including oxides (such as tunnel structure oxides and layered transition metal oxides), transition metal fluorides (typically FeF_3), polyanionic compounds (such as $NaFePO_4$, $NaVPO_4F$, $Na_3M_2(PO_4)_3$ NASICON compounds), Prussian blue analogues, and organic electrodes, have displayed outstanding sodium storage performance [3]. Meanwhile, significant progress has been achieved in the area of anodes for SIBs. It has been revealed that carbon materials, metals, alloys, and metal oxides/sulfides are promising anode materials for SIBs [4–6]. Among these materials, iron sulfides, such as FeS_2 [7–9], FeS [10] and $Fe_{1-x}S$ [11, 12], have attracted much attention due to their advantages of abundant reserves, non-toxicity, low cost, and high theoretical capacity (894 mAh g^{-1} for FeS_2, based on the conversion reaction of $FeS_2 + 4Na \leftrightarrow 2Na_2S + Fe$). However, the intrinsically low conductivity and notable volume change during the charge–discharge process greatly restrain its rate performance and cycling stability, restricting its further commercialization.

To solve these problems, Chen's group tuned an electrolyte and applied a higher voltage cutoff to improve the electrochemical performance of Na/FeS_2 and Li/FeS_2 cells [13, 14]. Numerous studies have revealed that constructing nanostructured materials can greatly reduce the electron/ion transport pathways and effectively buffer the large volume expansion during electrochemical processes, thus improving the reversibility and rate capability of FeS_2 anode materials [15, 16]. Moreover, the combination of a carbon or a polypyrrole (ppy) modification strategy to form a coating or an embedded structure (such as FeS_2/C [17–20], ppy@MoO_3 [21–23], ppy@V_2O_5 [24]) would help prevent aggregation and improve the conductivity of the electrode materials, thus enhancing the cycling and rate performance. For example, Liu et al. designed FeS_2@C nanoboxes and obtained discharge capacity of 511 mAh g^{-1} at 100 mA g^{-1} after 100 cycles [25]. Graphene is a highly conductive ultrathin nanosheet, with a large surface area and high flexibility, which is commonly used as modification material. In previous studies, FeS/reduced graphene oxide (rGO) [26], FeS_2/rGO [27], Fe_3O_4/rGO [28], Fe_2O_3/rGO [29], and $LiFePO_4$/rGO [30, 31] composites have been fabricated and used in lithium-ion batteries (LIBs). It is demonstrated that enwrapping anode materials in a conductive network is a favorable strategy to enhance the rate capability. However, the FeS_2/graphene composite with an enwrapping structure for SIBs has not been reported.

Here, we report a two-step method for the preparation of a novel rGO-wrapped FeS_2 (FeS_2/rGO) composite for SIBs. Structural and morphological characterization revealed that the FeS_2 nanoparticles are evenly surrounded in the interconnected rGO networks. The composite displayed superior sodium storage performance even at high charge–discharge current densities.

2 Experimental

2.1 Materials Synthesis

FeS_2/rGO was synthesized via a hydrothermal method, followed by a sulfurization process. All chemicals were of analytical grade and used without further purification.

Synthesis of Fe_3O_4/rGO composite In a typical synthesis, 0.04 g of graphene oxide was dispersed in 65 mL of deionized water by sonication. Then, 0.4 g of $Fe(NO_3)_3 \cdot 9H_2O$ was dissolved in the above suspension and stirred for 4 h at 70 °C. Following this, 5 mL of $N_2H_4 \cdot H_2O$ was added to the above system, and the solution was sealed in a 100-mL Teflon-lined stainless-steel autoclave for hydrothermal reaction at 150 °C for 6 h. Finally, the rGO-wrapped Fe_3O_4 composite was collected by centrifugation, washed with water and ethanol three times, and dried at 70 °C in a vacuum for 12 h.

Synthesis of FeS_2/rGO Composite The as-prepared Fe_3O_4/rGO and sulfur powder in a weight ratio of 1:2 were mixed and pressed into a small tablet and sealed in a small quartz tube under Ar atmosphere. Then, the quartz tube was heated at 150 °C for 2 h and subsequently at 550 °C for 6 h in a quartz tube reactor. After cooling down and washing with CS_2 to remove the residual sulfur powder, the final FeS_2/rGO composite was obtained. For comparison, FeS_2 nanoparticles were prepared using the same method without the addition of rGO.

2.2 Materials Characterization

The crystal structures of the as-prepared samples were characterized by powder X-ray diffraction (XRD) using Cu Ka radiation. The morphologies were investigated using field-emission scanning electron microscopy (SEM) on a JEOL JSM-7500FA system and transmission electron

microscopy (TEM) on a Philips Tecnai 20 (200 kV). TG thermal nitrogen adsorption–desorption isotherms of the samples were obtained on a Quantachrome Autosorb-IQ2 analyzer at 77 K. Specific surface areas were measured by Brunauer–Emmett–Teller (BET) analysis.

2.3 Electrochemical Measurements

Electrochemical measurements were conducted using CR2032 two-electrode coin cells, with sodium metal as the counter and reference electrodes and glass fiber as the separator. The working electrodes were made by pasting a slurry on copper foil, followed by drying in vacuum at 80 °C for 12 h. The slurry was prepared by mixing active materials, Super P, and carboxymethyl cellulose in the weight ratio of 8:1:1. A solution of 1 M $NaClO_4$ in ethylene carbonate/propylene carbonate (v/v = 1/1) with 5 wt% fluoroethylene carbonate additive was used as the electrolyte. Cyclic voltammetry (CV, 0–2.5 V, 0.1 mV s^{-1}) tests and electrochemical impendence spectroscopy (EIS, with 5 mV amplitude in a frequency range from 100 kHz to 0.01 Hz at open-circuit potential) tests were conducted on a Biologic VMP-3 electrochemical workstation. The galvanostatic charge–discharge curves, cycling performance, and rate capabilities of the electrode materials were tested on a LAND Battery Test System, in the voltage range of 0.01–2.3 V. All the tests were carried out at room temperature.

3 Results and Discussion

The crystal structures and morphologies of the as-prepared Fe_3O_4/rGO and Fe_3O_4 precursors are characterized by XRD, SEM, and TEM. From Fig. 1a, it can be seen that the main peaks in the XRD patterns are indexed to magnetite Fe_3O_4 (JCPDS card No. 75-0449). For the Fe_3O_4/rGO composite, a weak peak at about 22.5° is detected, which can be indexed to rGO. From Fig. 1b, c, one can see that both the precursors are mainly composed of uniform nanoparticles about 80 nm in diameter. Figure 1c shows that each nanoparticle is surrounded by thin graphene nanosheets. The TEM image shown in Fig. 1d further confirms the enwrapped structure of the composite. Moreover, it is obvious that each nanoparticle is connected by rGO to form an integral 3D network.

Figure 2 shows the crystal structure and morphologies of the as-prepared FeS_2 and FeS_2/rGO samples. As shown in Fig. 2a, both the samples show high-intensity XRD peaks, all of which can be indexed to pyrite FeS_2 (JCPDS card No. 06-0710), demonstrating the high purity and good crystallinity of the two samples. Figure 2b, c shows that the FeS_2 sample is composed of irregular particles like the Fe_3O_4 precursor. However, it can be observed that the particles tend to aggregate and become larger than the precursor, which is caused by the sulfuration process. Figure 2d shows that the general morphology of the FeS_2/rGO composite is similar to that of the Fe_3O_4/rGO precursor. The TEM image shown in Fig. 2e further reveals that the FeS_2 nanoparticles continue to be evenly dispersed in the graphene networks and that the particle size remains largely unchanged, compared to its precursor. Figure 2f shows that each nanoparticle is surrounded by graphene, which effectively prevents the aggregation of the FeS_2 nanoparticles. The thickness of the graphene layer is 2–3 nm (Fig. 2g). High-resolution TEM images (HRTEM, Fig. 2g, h) display clear lattice fringes with an interplane distance of 0.16 nm, corresponding to the (311) plane of pyrite FeS_2. The selected-area electron diffraction (SAED) pattern of FeS_2/rGO (Fig. 2i) shows well-defined rings, indicating that the as-prepared FeS_2 is polycrystalline.

According to the N_2 adsorption–desorption measurements (Fig. 3b), the specific surface areas of FeS_2 and FeS_2/rGO are 25.6 and 58.1 m^2 g^{-1}, respectively, indicating that the introduction of rGO significantly increases the surface areas. To determine the rGO content in the composite, thermogravimetric analysis is carried out in an air atmosphere (Fig. 3a). Both the samples display a minor weight loss (~ 6–8%) under 200 °C, which is due to the vapor of the residual water in the materials. Then a large weight loss of about 35% is observed in the range 400–500 °C for pure FeS_2, which corresponds to the conversion of FeS_2 to Fe_2O_3. (The theoretical weight loss is ~ 33.3%.) For FeS_2/rGO, a more significant weight loss of about 42% is observed between 400 and 600 °C, which may be caused by the phase change of FeS_2 to Fe_2O_3 and rGO to carbon dioxide. Based on the thermogravimetric analysis, the weight content of FeS_2 in the FeS_2/rGO composite can be calculated to be about 79.1%. According to the above analysis, the FeS_2/rGO composite contains integral nanostructures, with the FeS_2 nanoparticles enwrapped in the 3D rGO networks. This unique structure endows the composite with high structural stability and super electron conductivity, which may be beneficial for the cycling stability and rate performance of the FeS_2 electrode material for sodium storage.

Figure 4a, b shows the cyclic voltammetry (CV) curves of pure FeS_2 and the FeS_2/rGO composite at a scan rate of 0.1 mV s^{-1} between 0 and 2.5 V (vs. Na/Na^+). During the initial cathodic scan, a large peak appears at 1.0 V and a broad peak appears at 0.25 V for the FeS_2 electrode, which corresponds to Na^+ intercalation and the formation of the Na_xFeS_2 ($x < 2$) phase, Fe and Na_2S, and the formation of a solid-electrolyte interface (SEI) layer [13, 16, 32]. For the FeS_2/rGO electrode, a large peak at ~ 0.65 V and a small peak at ~ 0.1 V are detected, which may be due to a

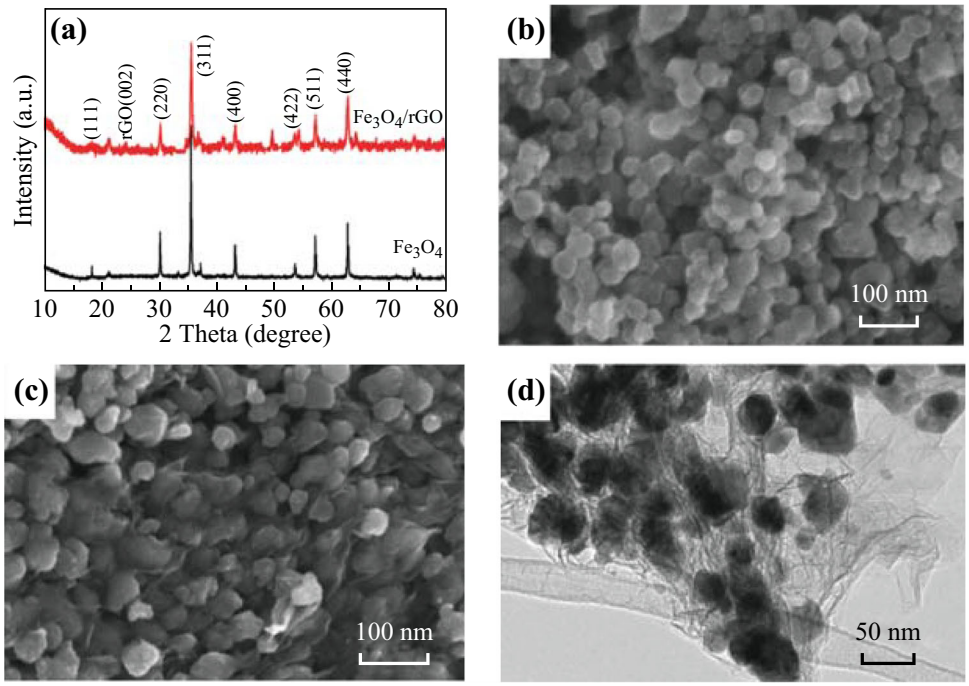

Fig. 1 **a** XRD patterns of the as-prepared Fe_3O_4 and Fe_3O_4/rGO precursors, **b** SEM image of Fe_3O_4, **c** SEM image, and **d** TEM image of Fe_3O_4/rGO

similar electrochemical process with the FeS_2 electrode. The differences in the peaks of the two samples may be caused by the nanostructure and the introduction of rGO. During the subsequent anodic scan, the peaks observed at ~ 1.4 and ~ 1.8 V can be attributed to be the desodiation process, with the formation of Na_2FeS_2 and $Na_{2-x}FeS_2$ [19]. During the subsequent cycles, the CV curves are quite different from those in the initial cycle, which may be due to the irreversible formation of the SEI layer and the decomposition of the electrolyte [19, 33–35]. It can be observed that the FeS_2/rGO electrode shows much better repeatability and a larger closed curve area than those of the pure FeS_2 electrode, demonstrating its much better cycling stability and higher specific capacities.

Figure 5a presents the charge–discharge curves of FeS_2/rGO electrode at a current density of 100 mA g^{-1}. An initial discharge plateau at ~ 1.0 V (vs. Na/Na^+) and charge plateau at ~ 1.3 V are observed, which are in good agreement with the CV curves. In the subsequent cycles, the charge–discharge curves do not change much, showing good electrochemical reversibility. The cycling performances of the two samples are further evaluated at 100 mA g^{-1}. As shown in Fig. 5b, both the electrodes have quite good cycling stability. However, the FeS_2/rGO electrode has obviously higher specific capacities than does the pure FeS_2 electrode, which may be due to the higher utilization of the active materials after the introduction of rGO. The FeS_2/rGO composite displays a high initial discharge capacity of 1263.2 mAh g^{-1} and charge capacity of 759.4 mAh g^{-1}, showing a low coulombic efficiency of 60.1%, which is mainly caused by the irreversible formation of the SEI layer and electrolyte decomposition in the initial cycle. Moreover, the dissolution of sodium polysulfides into organic liquid electrolytes causes a parasitic redox shuttle, leading to unfavorable side reactions with sodium, reducing the charging efficiency and resulting in serious capacity decay [36–38]. In the following cycles, the coulombic efficiency increases over 95%. From the second cycle, the discharge and charge capacities are stable and remain at 609.5 and 581.7 mAh g^{-1}, respectively, after 100 cycles.

The rate capability of the two FeS_2 electrodes is evaluated using varying current densities from 0.1 to 10 A g^{-1} and back to 0.1 A g^{-1}. As shown in Fig. 5c, the average specific capacities for FeS_2/rGO electrodes are 705, 672, 613, 555, 496, 426, and 344 mAh g^{-1} at 0.1, 0.2, 0.5, 1, 2, 5, and 10 A g^{-1}, respectively, which are remarkably higher than those for pure FeS_2 electrode, demonstrating its superior rate performance. When the current density is altered back to 0.1 A g^{-1}, the reversible capacity remains at ~ 655 mAh g^{-1} after 90 cycles, further confirming the excellent cycling stability of the FeS_2/rGO composite. We further investigate the electrode process kinetics of the two materials through EIS. As shown in Fig. 5d, both the Nyquist spectra are composed of a semicircle in the high-frequency region and an inclined line in the low-frequency region. The bigger semicircle for the FeS_2 electrode illustrates the poor electrical conductivity of the active

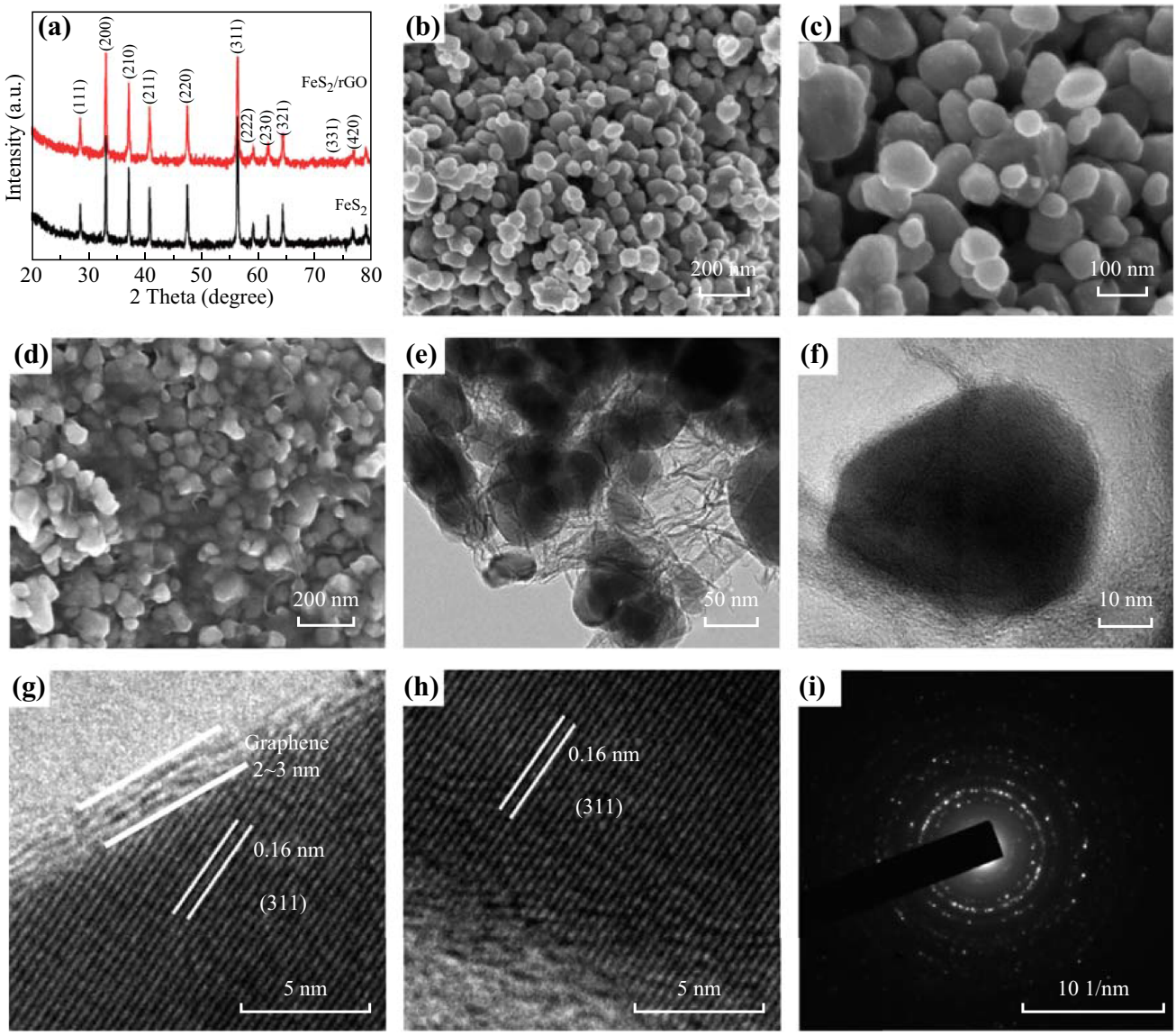

Fig. 2 **a** XRD patterns of the as-prepared FeS_2 and FeS_2/rGO composite, **b**, **c** SEM images of FeS_2, **d** SEM image, **e**, **f** TEM images, **g**, **h** HRTEM images, and **i** SAED pattern of FeS_2/rGO composite

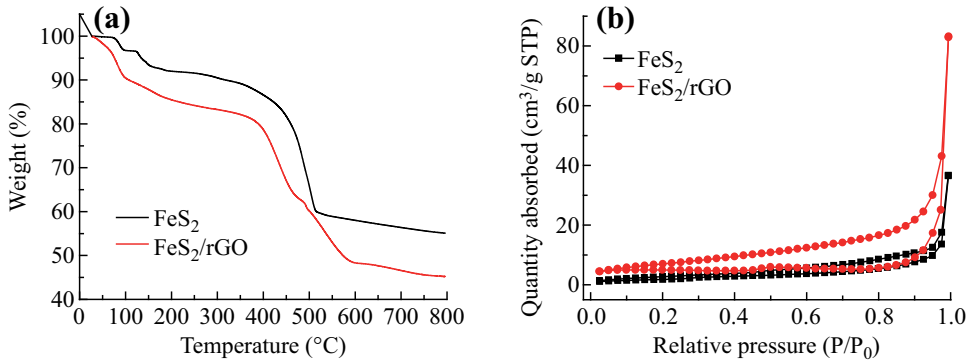

Fig. 3 **a** TG curves and **b** N_2 adsorption–desorption curves of FeS_2 and FeS_2/rGO composite

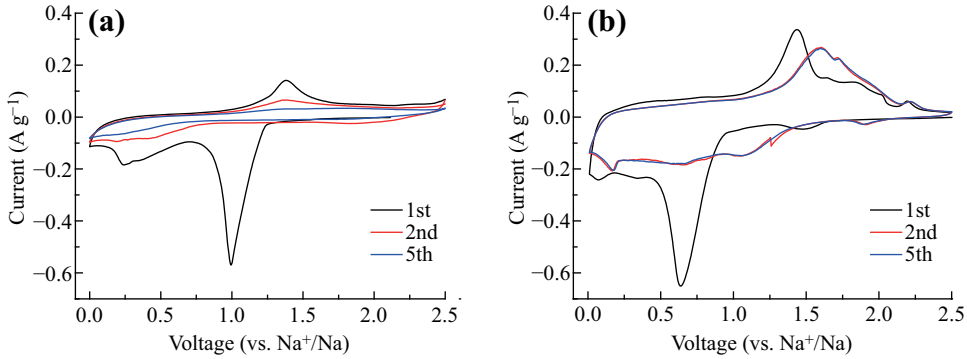

Fig. 4 CV curves of **a** FeS_2 and **b** FeS_2/rGO

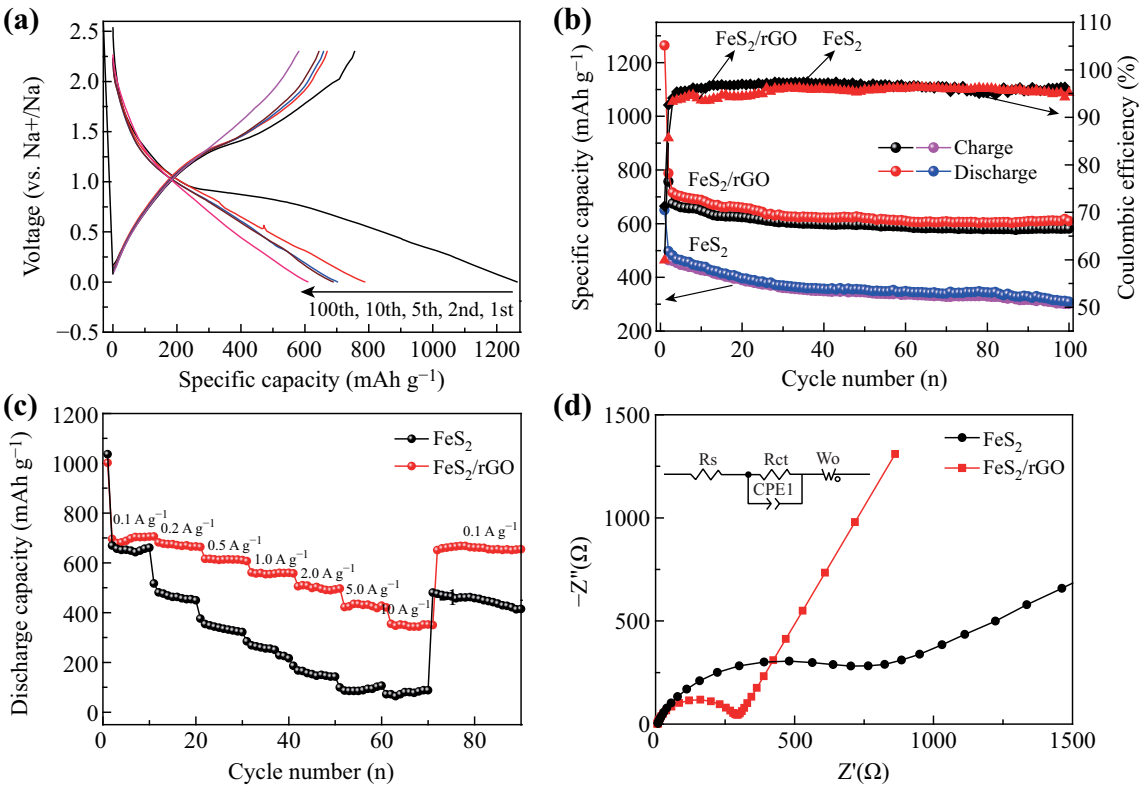

Fig. 5 **a** Galvanostatic charge–discharge curves of FeS_2/rGO, **b** cycle life and coulombic efficiencies, **c** rate performance, and **d** Nyquist plots for FeS_2 and FeS_2/rGO composite

materials. According to the Z-view program in the Sai software set, R_{ct} for FeS_2 and FeS_2/rGO electrodes is 1055.1 and 291.9 Ω, respectively, illustrating the better charge transfer kinetics of the FeS_2/rGO electrode.

The FeS_2/rGO composite displays much higher specific capacity and better rate capability than does the pure FeS_2 electrode. It is inferred that several features may contribute to the excellent electrochemical properties. First, the intimate contact of the FeS_2 nanoparticles with rGO and the integral conductive rGO networks provide a facile electron transport pathway, ensuring good rate performance [27, 30]. Second, the unique enwrapping structure can effectively improve the structural stability and buffer the volume change of FeS_2 during the charge–discharge process [26, 28]. To investigate the structural stability, the nanostructures of the freshly prepared FeS_2/rGO electrode and the FeS_2/rGO electrode after 100 cycles are investigated by SEM and TEM. From Fig. 6a, it can be seen that the morphology of the FeS_2/rGO composite does not change. After 100 sodiation–desodiation cycles, the nanoparticles are not very regular but are still enwrapped in the graphene networks (Fig. 6b, c). The high-resolution TEM test shows that the nanoparticles transform into smaller nanocrystals (Fig. 6d), which are still surrounded

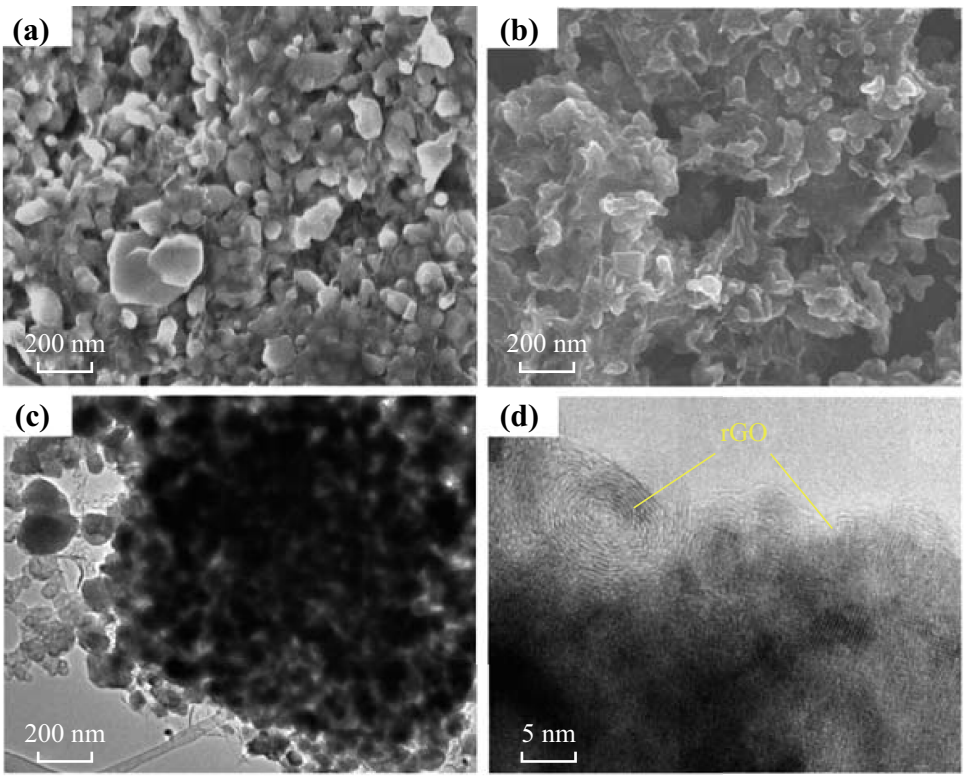

Fig. 6 **a** SEM image of freshly prepared FeS_2/rGO electrode, **b** SEM image, and **c**, **d** TEM images of FeS_2/rGO electrode after 100 charge–discharge cycles

by rGO. It is obvious that the graphene network can effectively prevent the collapse of the structure and the aggregation of FeS_2 nanoparticles, thus improving the cycling stability of the FeS_2/rGO composite. Moreover, the improvement of the BET surface area increases the contact area between the active material and the electrolyte, which helps improve the utilization of active materials, endowing the FeS_2/rGO composite with high specific capacitance.

4 Conclusions

In summary, an rGO-wrapped FeS_2 composite has been successfully synthesized via a hydrothermal method, followed by sulfuration, and used as an anode for SIBs. The well-dispersed rGO constructs 3D conductive networks and markedly increases the BET surface area and conductivity of the FeS_2 nanoparticles. Thus, the FeS_2/rGO composite displays an initial discharge capacity of 1263.2 mAh g^{-1} at 100 mA g^{-1} and a high discharge capacity of 344 mAh g^{-1} at 10 A g^{-1}. Moreover, the enwrapping structure helps in preventing the aggregation of the FeS_2 nanoparticles during the electrochemical process, contributing to the excellent cycling stability. After 100 cycles, the discharge capacity is 609.5 mAh g^{-1}. We believe that our strategy could be extended to the fabrication of other high-performance metal sulfide/rGO composites for LIBs or SIBs.

Acknowledgements This work was supported by National Natural Science Foundation of China (51702138, 51702079), Natural Science Foundation of Jiangsu Province (BK20160213), and the Priority Academic Program Development of Jiangsu Higher Education Institutions.

References

1. V. Palomares, P. Serras, I. Villaluenga, K.B. Hueso, J. Carretero-Gonzalez, T. Rojo, Na-ion batteries, recent advances and present challenges to become low cost energy storage systems. Energy Environ. Sci. **5**(3), 5884–5901 (2012). https://doi.org/10.1039/c2ee02781j
2. J. Goodenough, Y. Kim, Challenges for rechargeable Li batteries. Chem. Mater. **22**(3), 587–603 (2010). https://doi.org/10.1021/cm901452z
3. H. Kim, H. Kim, Z. Ding, M. Lee, K. Lim, G. Yoon, K. Kang, Recent progress in electrode materials for sodium-ion batteries.

Adv. Energy Mater. **6**(19), 1600943 (2016). https://doi.org/10.1002/aenm.201600943
4. N. Yabuuchi, K. Kubota, M. Dahbi, S. Komaba, Research development on sodium-ion batteries. Chem. Rev. **114**(23), 11636 (2014). https://doi.org/10.1021/cr500192f
5. M.L. Kou, Y. Liu, C. Zhang, L. Shao, Z. Tian, Z. Deng, C. Gao, A mini review on nanocarbon-based 1D macroscopic fibers: assembly strategies and mechanical properties. Nano-Micro Lett. **9**, 51 (2017). https://doi.org/10.1007/s40820-017-0151-7
6. H. Kang, Y. Liu, K. Cao, Y. Zhao, L. Jiao, Y. Wang, H. Yuan, Update on anode materials for Na-ion batteries. J. Mater. Chem. A **3**(35), 17899–17913 (2015). https://doi.org/10.1039/C5TA03181H
7. K. Zhang, M. Park, L. Zhou, G. Lee, J. Shin, Z. Hu, S.L. Chou, J. Chen, Y.M. Kang, Cobalt-doped FeS_2 nanospheres with complete solid solubility as a high-performance anode material for sodium-ion batteries. Angew. Chem. Int. Ed. **55**(41), 12822–12826 (2016). https://doi.org/10.1002/anie.201607469
8. S. Zhang, The redox mechanism of FeS_2 in non-aqueous electrolytes for lithium and sodium batteries. J. Mater. Chem. A **3**(15), 7689–7694 (2015). https://doi.org/10.1039/C5TA00623F
9. Y. Xiao, S. Lee, Y. Sun, The application of metal sulfdes in sodium ion batteries. Adv. Energy Mater. **7**(3), 1601329 (2016). https://doi.org/10.1002/aenm.201601329
10. X. Wei, W. Li, J. Shi, L. Gu, Y. Yu, FeS@C on carbon cloth as flexible electrode for both lithium and sodium storage. ACS Appl. Mater. Interfaces. **7**(50), 27804–27809 (2015). https://doi.org/10.1021/acsami.5b09062
11. L. Li, S. Peng, N. Bucher, H. Chen, N. Shen et al., Large-scale synthesis of highly uniform $Fe_{1-x}S$ nanostructures as a high-rate anode for sodium ion batteries. Nano Energy **37**, 81–90 (2017). https://doi.org/10.1016/j.nanoen.2017.05.012
12. Y. Xiao, J. Hwang, I. Belharouak, Y. Sun, Na-storage capability investigation of carbon nanotubes-encapsulated $Fe_{1-x}S$ composite. ACS Energy Lett. **2**(2), 364–372 (2017). https://doi.org/10.1021/acsenergylett.6b00660
13. Z. Hu, Z. Zhu, F. Cheng, K. Zhang, J. Wang, C. Chen, J. Chen, Pyrite FeS_2 for high-rate and long-life rechargeable sodium batteries. Energy Environ. Sci. **8**(4), 1309–1316 (2015). https://doi.org/10.1039/C4EE03759F
14. Z. Hu, K. Zhang, Z. Zhu, Z. Tao, J. Chen, FeS_2 microspheres with an ether-based electrolyte for high-performance rechargeable lithium batteries. J. Mater. Chem. A **3**(24), 12898–12904 (2015). https://doi.org/10.1039/C5TA02169C
15. M. Walter, T. Zünd, M. Kovalenko, Pyrite (FeS_2) nanocrystals as inexpensive high performance lithium-ion cathode and sodium-ion anode materials. Nanoscale **7**(20), 9158–9163 (2015). https://doi.org/10.1039/C5NR00398A
16. A. Douglas, R. Carter, L. Oakes, K. Share, A. Cohn, C. Pint, Ultrafine iron pyrite (FeS_2) nanocrystals improve sodium-sulfur and lithium-sulfur conversion reactions for efficient batteries. ACS Nano **9**(11), 11156–11165 (2015). https://doi.org/10.1021/acsnano.5b04700
17. B. Wu, H. Song, J. Zhou, X. Chen, Iron sulfide-embedded carbon microsphere anode material with high-rate performance for lithium-ion batteries. Chem. Commun. **47**(30), 8653–8655 (2011). https://doi.org/10.1039/c1cc12924d
18. D. Zhang, Y. Mai, J. Xiang, X. Xia, Y. Qiao, J. Tu, FeS_2/C composite as an anode for lithium ion batteries with enhanced reversible capacity. J. Power Sources **217**(11), 229–235 (2012). https://doi.org/10.1016/j.jpowsour.2012.05.112
19. Y. Wang, J. Yang, S. Chou, H. Liu, W. Zhang, D. Zhao, S.X. Dou, Uniform yolk-shell iron sulfide-carbon nanospheres for superior sodium-iron sulfide batteries. Nat. Commun. **6**, 8689–8697 (2015). https://doi.org/10.1038/ncomms9689
20. L. Liu, Z. Yuan, C. Qiu, J. Liu, A novel FeS_2/CNT microspherical cathode material with enhanced electrochemical characteristics for lithium-ion batteries. Solid State Ion. **241**, 25–29 (2013). https://doi.org/10.1016/j.ssi.2013.03.031
21. F. Yu, Y. Liu, Y. Zhu, F. Dai, L. Zhang, Z. Wen, Polypyrrole@MoO_3/reductive graphite oxide nanocomposites as anode material for aqueous supercapacitors with high performance. Mater. Lett. **171**, 104–107 (2016). https://doi.org/10.1016/j.matlet.2016.01.028
22. Y. Liu, B. Zhang, Y. Yang, Z. Chang, Z. Wen, Y. Wu, Polypyrrole-coated α-MoO_3 nanobelts with good electrochemical performance as anode material for aqueous supercapacitor. J. Mater. Chem. A **1**(43), 13582–13587 (2013). https://doi.org/10.1039/c3ta12902k
23. Y. Liu, B. Zhang, S. Xiao, L. Liu, Z. Wen, Y. Wu, A nanocomposite of MoO_3 coated with PPy as an anode material for aqueous sodium rechargeable batteries with excellent electrochemical performance. Electrochim. Acta **116**(2), 512–517 (2014). https://doi.org/10.1016/j.electacta.2013.11.077
24. Q. Qu, Y. Zhu, X. Gao, Y. Wu, Core-shell structure of polypyrrole grown on V_2O_5 nanoribbon as high performance anode material for supercapacitors. Adv. Energy Mater. **2**, 950–955 (2012). https://doi.org/10.1002/aenm.201200088
25. Z. Liu, T. Lu, T. Song, X. Yu, X. Lou, U. Paik, Structure-designed synthesis of FeS_2@C yolk-shell nanoboxes as a high-performance anode for sodium-ion batteries. Energy Environ. Sci. **10**(7), 1576–1580 (2017). https://doi.org/10.1039/C7EE01100H
26. L. Fei, Q. Lin, B. Yuan, G. Chen, P. Xie et al., Reduced graphene oxide wrapped FeS nanocomposite for lithium ion battery anode with improved performance. ACS Appl. Mater. Interfaces. **5**(11), 5330–5335 (2013). https://doi.org/10.1021/am401239f
27. X. Wen, X. Wei, L. Yang, P. Shen, Self-assembled FeS_2 cubes anchored on reduced graphene oxide as an anode material for lithium ion batteries. J. Mater. Chem. A **3**(5), 2090–2096 (2015). https://doi.org/10.1039/C4TA05575F
28. G. Zhou, D. Wang, F. Li, L. Zhang, N. Li, Z. Wu, L. Wen, G.Q. Lu, H.M. Chen, Graphene-wrapped Fe_3O_4 anode material with improved reversible capacity and cyclic stability for lithium ion batteries. Chem. Mater. **22**(18), 5306–5313 (2010). https://doi.org/10.1021/cm101532x
29. Z. Zhang, Y. Wang, S. Chou, H. Li, H. Liu, J. Wang, Rapid synthesis of α-Fe_2O_3/rGO nanocomposites by microwave autoclave as superior anodes for sodium-ion batteries. J. Power Sources **280**, 107–113 (2015). https://doi.org/10.1016/j.jpowsour.2015.01.092
30. H. Wu, Q. Liu, S. Guo, Composites of graphene and $LiFePO_4$ as cathode materials for lithium-ion battery: a mini-review. Nano-Micro Lett. **6**(4), 316–326 (2014). https://doi.org/10.1007/s40820-014-0004-6
31. B. Hu, F. Wu, C. Lin, A. Khlobystov, L. Li, Graphene-modified $LiFePO_4$ cathode for lithium ion battery beyond theoretical capacity. Nat. Commun. **4**, 1687–1693 (2013). https://doi.org/10.1038/ncomms2705
32. Y. Zhu, L. Suo, T. Gao, X. Fan, F. Han, C. Wang, Ether-based electrolyte enabled Na/FeS_2 rechargeable batteries. Electrochem. Commun. **54**, 18–22 (2015). https://doi.org/10.1016/j.elecom.2015.02.006
33. H. Hou, M. Jing, Y. Yang, Y. Zhu, L. Fang, W. Song, C. Pan, X. Yang, X. Ji, Sodium/lithium storage behavior of antimony hollow nanospheres for rechargeable batteries. ACS Appl. Mater. Interfaces **6**, 16189–16196 (2014). https://doi.org/10.1021/am504310k
34. Y. Ko, Y. Kang, Electrochemical properties of ultrafine Sb nanocrystals embedded in carbon microspheres for use as Na-ion battery anode materials. Chem. Commun. **50**, 12322–12324 (2014). https://doi.org/10.1039/C4CC05275G

35. Y. Luo, M. Balogun, W. Qiu, R. Zhao, P. Liu, Y. Tong, Sulfurization of FeOOH nanorods on a carbon cloth and their conversion into Fe_2O_3/Fe_3O_4-S core-shell nanorods for lithium storage. Chem. Commun. **51**, 13016–13019 (2015). https://doi.org/10.1039/C5CC04700E
36. T. Evans, D. Piper, S. Kim, S. Han, V. Bhat, K. Oh, S. Lee, Ionic liquid enabled FeS_2 for high-energy-density lithium-ion batteries. Adv. Mater. **26**, 7386–7392 (2014). https://doi.org/10.1002/adma.201402103
37. Y. Zhu, X. Fan, L. Suo, C. Luo, T. Gao, C. Wang, Electrospun FeS_2@carbon fiber electrode as a high energy density cathode for rechargeable lithium batteries. ACS Nano **10**, 1529–1538 (2016). https://doi.org/10.1021/acsnano.5b07081
38. T. Yersak, H. Macpherson, S. Kim, V. Le, C. Kang et al., Solid state enabled reversible four electron storage. Adv. Energy Mater. **3**, 120–127 (2013). https://doi.org/10.1002/aenm.201200267